nature physics

Article

https://doi.org/10.1038/s41567-023-02319-6

Inverse design of high-dimensional quantum optical circuits in a complex medium

In the format provided by the authors and unedited

Supplementary information for: Inverse-design of high-dimensional quantum optical circuits in a complex medium

The following supplementary information is provided: details of the high-dimensionally entangled two-photon source are presented in S.1, while the experimental estimation of success probability and optical losses is discussed in S.2. Detailed results on the manipulation of high-dimensionally entangled states in dimensions ($d = 2, 3, 5, 7$) using various types of gates in the macro-pixel and the orbital-angular-momentum (OAM) bases are presented in S.3. Furthermore, the independent characterization of our measurement apparatus and its effect on errors in QST and AA-QPT are reported in S.4 and S.5. A brief discussion of the misestimation of the initial state in linear inversion is presented in S.6. Finally, numerical results on the programmability and scalability of our gates and the effect of randomness and symmetry of mode-mixers on the gate performance are reported in S.7 and S.8.

S.1. High-dimensional two-photon entanglement source

The high-dimensional spatially entangled two-photon state is generated via degenerate Type-II spontaneous parametric downconversion (SPDC) by pumping a 15-mm long periodically poled Potassium Titanyl Phosphate (ppKTP) crystal with a 405nm continuous-wave laser. After passing through the long-pass dichroic filter and the band-pass filter, the signal and idler photons are separated using a polarising-beam-splitter (PBS) and are mapped on to the liquid-crystal-on-silicon-based spatial light modulators (SLM) (P_1 and P_3) which are placed in the Fourier plane of the ppKTP crystal. The main characteristics of the entanglement source, i.e., the strength of transverse-momentum correlation, generated beam waist, and the position of the beams, are determined by using our developed $2D\pi$-measurement [1], which involves the joint coincidence measurement of local π-phase step knife-edge scans across the SLMs at each party. The two-photon state is then characterised via quantum state tomography (See Methods) and the entanglement dimensionality is certified [2] using a high-dimensional entanglement witness in two discrete spatial-mode bases—the Macro-pixel basis [3] and the orbital-angular-momentum (OAM) basis [4]. We utilise these two bases as the set of input target modes for constructing the programmable circuits. For the macro-pixel basis, the size of pixels and their spacing are determined by the joint transverse momentum amplitude (JTMA) [1]. For the OAM basis, the set of modes are $\{|-\ell\rangle, \ldots, |0\rangle, \ldots, |\ell\rangle\}$ when the dimension of the circuit d is odd, otherwise $\{|-\ell\rangle, \ldots, |-1\rangle, |1\rangle, \ldots, |\ell\rangle\}$. The measured quantifiers of the generated high-dimensionally entangled two-photon states are reported in Table S.1 and the reconstructed density matrices are depicted in Fig. S.1 and Fig. S.2 for the macro-pixel and OAM bases, respectively.

Table S.1: Generated high-dimensionally entangled two-photon states: State purity $\mathcal{P}$, Entanglement dimensionality d_{ent}, Fidelity to maximally entangled state $\mathcal{F}$, Entanglement of Formation (E_{oF}). The reported errors are due to misalignment of measurement apparatus as well as photon counting statistics as discussed in S.5.

Basis	Dimension (d)	$\mathcal{P}$	d_{ent}	$\mathcal{F}(\rho^{(\text{in})}, \rho^{+})$	E_{oF} (ebits)
Macro-Pixel	2	96.7 ± 0.2 %	2	96.8 ± 1.4 %	0.798 ± 0.042
	3	92.6 ± 0.2 %	3	95.3 ± 0.4 %	1.231 ± 0.013
	5	88.8 ± 0.1 %	5	91.6 ± 0.6 %	1.510 ± 0.021
	7	75.1 ± 1.5 %	6	83.0 ± 1.2 %	1.194 ± 0.012
OAM	2	97.7 ± 0.4 %	2	97.5 ± 0.2 %	0.812 ± 0.001
	3	85.9 ± 0.2 %	3	90.8 ± 0.6 %	1.113 ± 0.014
	5	83.2 ± 0.1 %	5	86.5 ± 0.7 %	1.194 ± 0.019
	7	80.0 ± 0.1 %	6	80.6 ± 0.6 %	1.109 ± 0.016

S.2. Experimental estimation of success probability and optical losses

In the experiment, the measurements of success probability and overall transmittance are performed in the macro-pixel input basis. The results are shown in Fig. S.3 where the averaged optical transmittance is 0.051 ± 0.008,

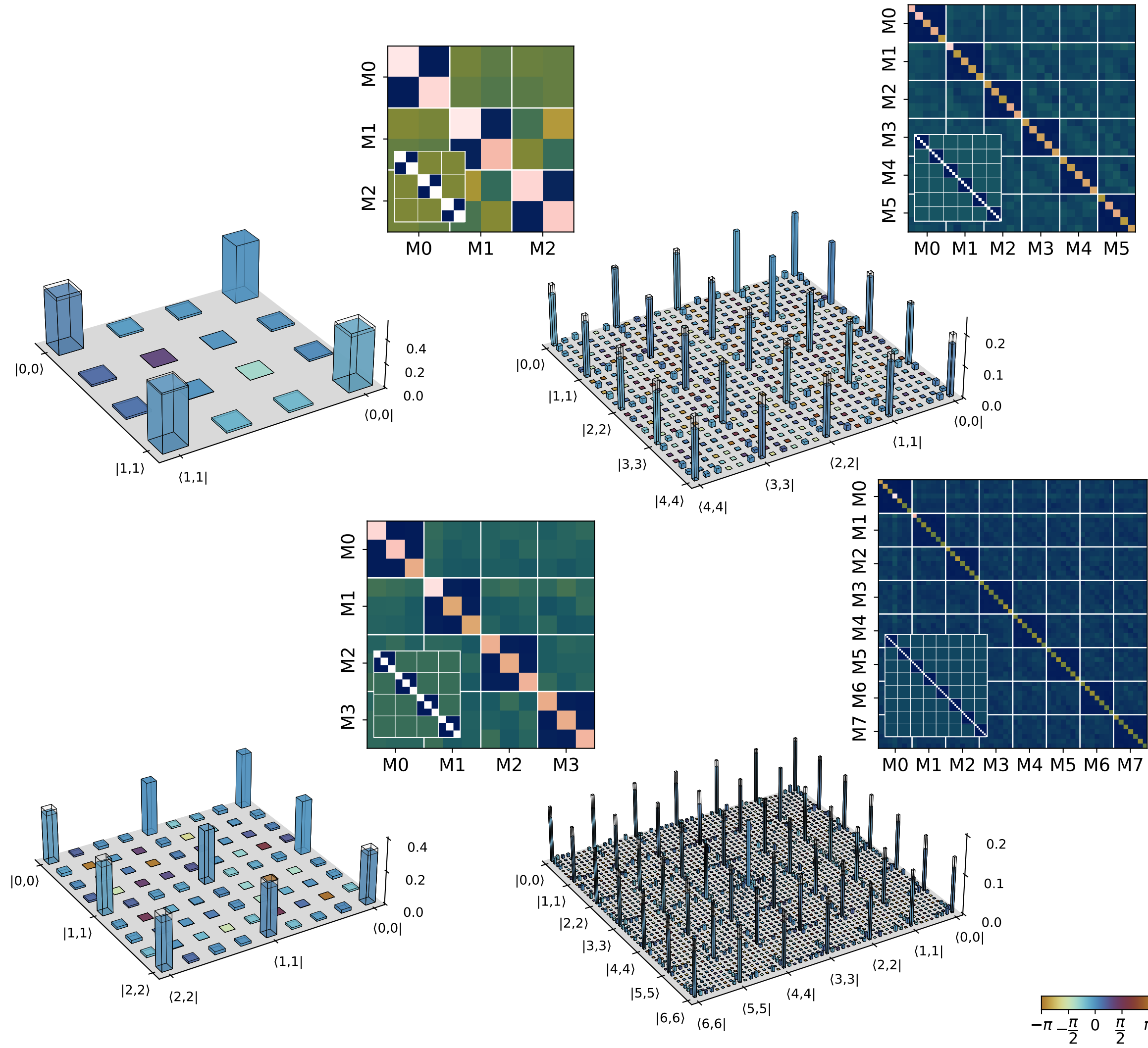

Figure S.1. **Generated high-dimensional entangled two-photon states in the macro-pixel basis.** Measured coincidence counts in all mutually unbiased bases (MUBs) and reconstructed density matrices via quantum state tomography in dimensions, $d = [2, 3, 5, 7]$. The amplitude and phase of density matrix elements are represented by the height of the bars and their colour, respectively. The ideal amplitude is represented by a transparent bar overlaid on the experimental result.

0.040 ± 0.006, 0.026 ± 0.004, and 0.028 ± 0.003 for 2, 3, 5, and 7-dimensional gates respectively. We measure the success probability for 3 randomly chosen implementations of Fourier-$\mathbb{F}$ gates in $2, 3$, and 5 dimensions and observe an $\mathcal{S}$ of 0.36 ± 0.014, 0.27 ± 0.03, and 0.18 ± 0.04, respectively. We thus infer an average optical transmittance of $\mathcal{T}_o = 0.14 \pm 0.02$ which is attributed to the optical insertion and propagation losses, diffraction efficiency of the two SLMs, and other interface losses at the lenses and mirrors. We note that the main contribution to the loss is due to the success probability arising from control of only a single polarisation channel of the multi-mode fiber, which can be further improved when all polarisation-spatial modes of the optical system are controlled.

S.3. Manipulation of high-dimensional spatially entangled states

To study the programmabiltiy of our quantum circuits, we program many types of unitary gates, namely, the identity-$\mathbb{I}$, Pauli-$\mathbb{Z}$, Pauli-$\mathbb{X}$, Fourier-$\mathbb{F}$, and random unitaries-$\mathbb{R}$, in $2, 3, 5$, and 7 dimensions in both the macro-pixel and OAM input bases. For each implementation, we randomly appoint a set of target output foci to encode the circuit with. We then use these circuits to locally transform the d-dimensional spatially entangled two-photon state, which is then characterised by performing AA-QPT.

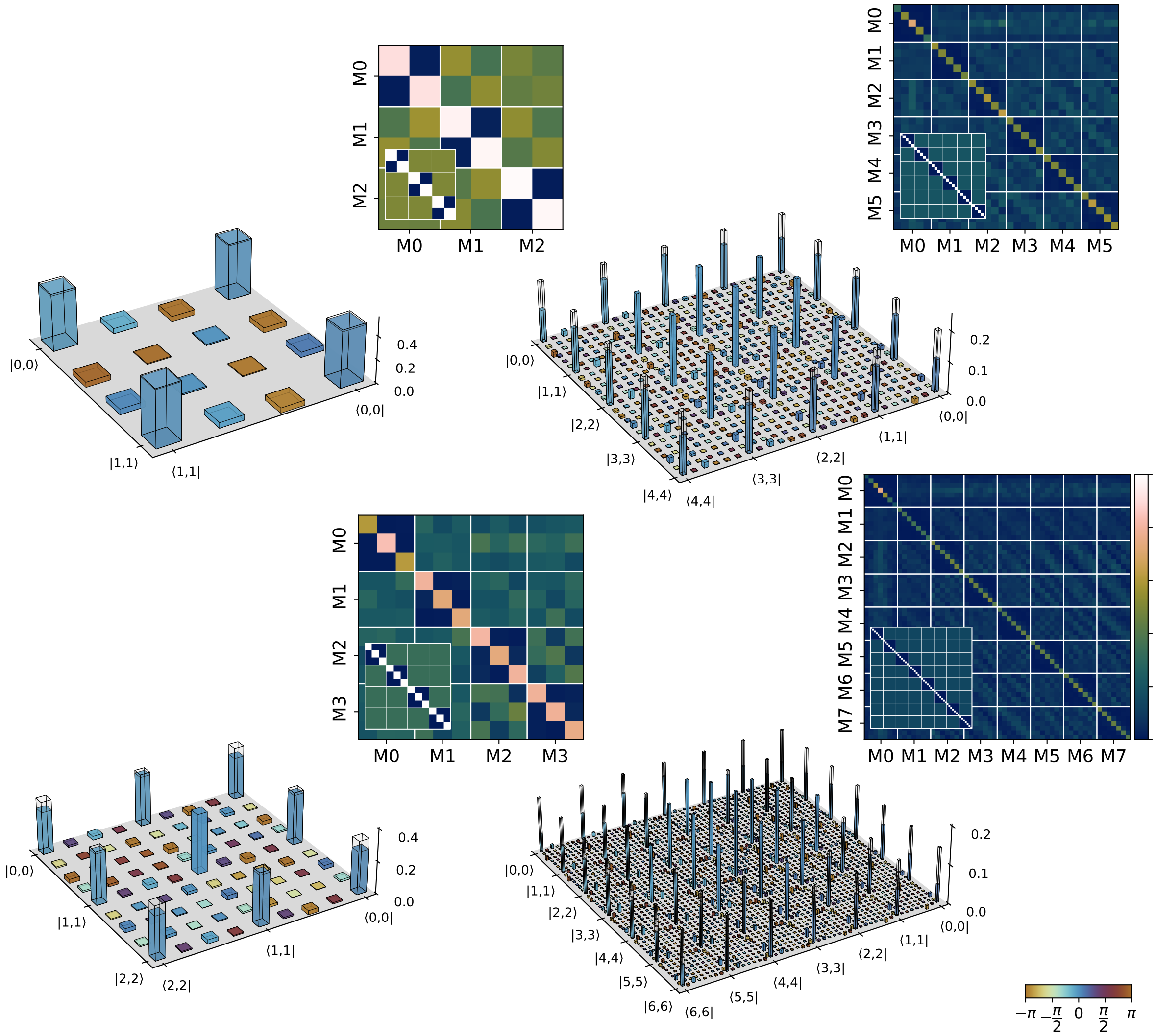

Figure S.2. **Generated high-dimensionally entangled two-photon states in the OAM basis.** Measured coincidence counts in all mutually unbiased bases (MUBs) and reconstructed density matrices via quantum state tomography in dimensions, $d = [2, 3, 5, 7]$. The amplitude and phase of density matrix elements are represented by the height of the bars and their colour, respectively. The ideal amplitude is represented by a transparent bar overlaid on the experimental result.

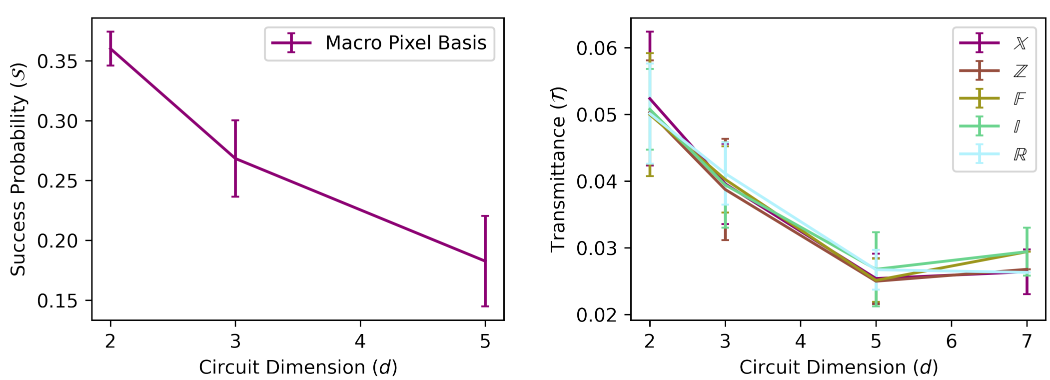

Figure S.3. Success probability (left) and optical transmittance (right) in macro-pixel input basis.

Table S.2 shows the fidelity and purity of the best-case gates in each dimension. The measured tomography data and reconstructed density matrices of these processes are shown in Figs. S.5 and S.6 for the macro-pixel and OAM bases. The process fidelity quantifies how close to ideal our gates are, taking into account the non-maximally entangled nature of the input state. As a separate metric, the fidelities of the output state to an ideal transformed state allows independent verification that the gates preserve high-dimensional entanglement. Tables S.3 and S.4 show the output state fidelity, purity, and entangement dimensionality for all best-case gates.

In theory, the process fidelity of a circuit in a given dimension should be independent of the type of circuit and input/output modes used. In practice, however, experimental imperfections relating to the measurement apparatus and characterisation of the MMF result in a spread of fidelities with a lower average over all circuit instances, which are reported in Table. S.5. This shows the average fidelities and purities of circuits for various types of gates sampled over different sets of output foci. The histogram of fidelities of all the implemented gates are shown in Fig. S.4.

Table S.2: Fidelity $\mathcal{F}$ and purity $\mathcal{P}$ of the channel, $\widetilde{\rho_{\xi*}}$ implemented by a gate $\mathbb{T}$ in d dimensions in the macro-pixel and OAM bases corresponding to the results presented in Fig. S.5 and S.6. The reported errors are due to misalignment of measurement apparatus as well as photon counting statistics as discussed in S.5.

Basis	$\mathbb{T}$	$\mathcal{F}(\widetilde{\rho_{\xi*}}, \rho_\xi)$				$\mathcal{P}(\widetilde{\rho_{\xi*}})$			
		$d=2$	$d=3$	$d=5$	$d=7$	$d=2$	$d=3$	$d=5$	$d=7$
Macro-Pixel	$\mathbb{I}$	96.7 ± 0.9 %	97.4 ± 0.7 %	88.0 ± 0.7 %	71.9 ± 1.1 %	94.5 ± 0.4 %	99.5 ± 0.3 %	95.4 ± 0.4 %	74.7 ± 1.2 %
	$\mathbb{Z}$	97.7 ± 0.9 %	96.1 ± 0.5 %	80.6 ± 1.0 %	65.2 ± 1.0 %	96.3 ± 0.4 %	99.5 ± 0.3 %	93.6 ± 0.5 %	77.5 ± 1.0 %
	$\mathbb{X}$	97.6 ± 0.8 %	95.0 ± 0.7 %	79.2 ± 1.0 %	60.1 ± 1.0 %	95.4 ± 0.4 %	97.5 ± 0.4 %	91.9 ± 0.6 %	82.6 ± 1.3 %
	$\mathbb{F}$	95.7 ± 0.9 %	89.3 ± 0.8 %	76.9 ± 1.1 %	58.9 ± 0.7 %	93.8 ± 0.5 %	88.3 ± 0.5 %	84.6 ± 0.6 %	75.1 ± 1.5 %
	$\mathbb{R}$	96.8 ± 0.7 %	91.8 ± 0.8 %	80.1 ± 1.1 %	63.5 ± 0.7 %	95.4 ± 0.3 %	91.3 ± 0.3 %	83.8 ± 0.5 %	77.3 ± 1.4 %
OAM	$\mathbb{I}$	91.2 ± 0.4 %	89.8 ± 0.7 %	76.6 ± 1.0 %	56.9 ± 0.9 %	92.2 ± 0.2 %	92.1 ± 0.4 %	83.1 ± 0.3 %	61.5 ± 0.4 %
	$\mathbb{Z}$	91.0 ± 0.4 %	87.0 ± 0.6 %	79.1 ± 0.6 %	54.2 ± 1.0 %	91.5 ± 0.2 %	87.3 ± 0.3 %	83.3 ± 0.3 %	61.2 ± 0.3 %
	$\mathbb{X}$	95.0 ± 0.5 %	91.0 ± 0.5 %	74.4 ± 0.9 %	53.0 ± 0.9 %	93.9 ± 0.3 %	94.3 ± 0.3 %	82.7 ± 0.3 %	61.4 ± 0.3 %
	$\mathbb{F}$	93.3 ± 0.4 %	87.9 ± 0.5 %	75.3 ± 0.7 %	57.4 ± 0.7 %	94.6 ± 0.2 %	87.9 ± 0.2 %	81.3 ± 0.3 %	62.3 ± 0.3 %
	$\mathbb{R}$	92.2 ± 0.5 %	84.9 ± 0.8 %	72.3 ± 0.9 %	51.7 ± 1.2 %	91.4 ± 0.3 %	88.2 ± 0.3 %	81.2 ± 0.3 %	64.1 ± 0.3 %

Table S.3: Fidelity $\mathcal{F}$ and purity $\mathcal{P}$ of the output state $\widetilde{\rho_{\xi*}^{(out)}}$, after being operated on by gate $\mathbb{T}$ in d dimensions in the macro-pixel and OAM bases. These results correspond to the data and density matrices presented in Fig. S.5 and S.6. The reported errors are due to misalignment of measurement apparatus as well as photon counting statistics as discussed in S.5.

Basis	$\mathbb{T}$	$\mathcal{F}(\widetilde{\rho_{\xi*}^{(\mathrm{out})}}, \rho_\xi)$				$\mathcal{P}(\widetilde{\rho_{\xi*}^{(\mathrm{out})}})$			
		$d=2$	$d=3$	$d=5$	$d=7$	$d=2$	$d=3$	$d=5$	$d=7$
Macro-Pixel	$\mathbb{I}$	95.6 ± 1.2 %	95.6 ± 0.8 %	85.3 ± 0.7 %	69.0 ± 0.8 %	96.4 ± 0.4 %	97.8 ± 0.3 %	91.4 ± 0.4 %	70.3 ± 0.9 %
	$\mathbb{Z}$	97.5 ± 1.1 %	95.9 ± 0.7 %	80.8 ± 0.9 %	58.1 ± 0.5 %	97.9 ± 0.5 %	99.5 ± 0.3 %	90.3 ± 0.5 %	68.0 ± 0.6 %
	$\mathbb{X}$	96.3 ± 1.0 %	93.8 ± 0.8 %	77.3 ± 0.9 %	53.9 ± 0.8 %	96.5 ± 0.4 %	97.1 ± 0.4 %	91.3 ± 0.5 %	70.0 ± 0.4 %
	$\mathbb{F}$	93.0 ± 0.8 %	87.6 ± 0.8 %	76.7 ± 0.8 %	55.2 ± 0.6 %	92.2 ± 0.4 %	85.5 ± 0.4 %	80.4 ± 0.4 %	69.5 ± 0.6 %
	$\mathbb{R}$	93.4 ± 0.7 %	89.2 ± 0.9 %	76.7 ± 0.6 %	61.8 ± 0.6 %	92.9 ± 0.3 %	88.7 ± 0.3 %	83.1 ± 0.4 %	70.8 ± 0.5 %
OAM	$\mathbb{I}$	92.0 ± 0.3 %	83.7 ± 0.7 %	75.6 ± 1.0 %	55.6 ± 0.7 %	91.4 ± 0.2 %	83.8 ± 0.2 %	77.5 ± 0.3 %	70.8 ± 0.2 %
	$\mathbb{Z}$	92.9 ± 0.4 %	82.2 ± 0.5 %	76.1 ± 0.5 %	51.8 ± 0.5 %	91.5 ± 0.2 %	81.1 ± 0.2 %	78.5 ± 0.2 %	71.6 ± 0.2 %
	$\mathbb{X}$	93.7 ± 0.4 %	86.2 ± 0.5 %	73.0 ± 0.6 %	51.1 ± 0.8 %	92.4 ± 0.2 %	84.1 ± 0.2 %	79.1 ± 0.2 %	74.5 ± 0.2 %
	$\mathbb{F}$	93.9 ± 0.4 %	84.3 ± 0.5 %	75.7 ± 0.3 %	58.6 ± 0.4 %	93.5 ± 0.2 %	79.7 ± 0.2 %	77.5 ± 0.2 %	71.6 ± 0.2 %
	$\mathbb{R}$	92.0 ± 0.5 %	83.4 ± 0.3 %	68.9 ± 0.5 %	50.4 ± 0.3 %	91.6 ± 0.2 %	80.8 ± 0.2 %	78.0 ± 0.2 %	74.2 ± 0.2 %

Table S.4: Entanglement dimensionality of the output state $\widetilde{\rho^{(out)}_{\xi*}}$, after being operated on by gate $\mathbb{T}$ in d dimensions in the macro-pixel and OAM bases. These results correspond to the data and density matrices presented in Fig. S.5 and S.6. The reported errors in dimensionality are based on the errors in fidelity reported in Table S.3.

$\mathbb{T}$	$d_{(\mathrm{ent})}(\widetilde{\rho^{(\mathrm{out})}_{\xi*}})$							
	Macro-Pixel				OAM			
	$d=2$	$d=3$	$d=5$	$d=7$	$d=2$	$d=3$	$d=5$	$d=7$
$\mathbb{I}$	2^{+0}_{-0}	3^{+0}_{-0}	5^{+0}_{-0}	5^{+1}_{-0}	2^{+0}_{-0}	3^{+0}_{-0}	4^{+0}_{-0}	4^{+1}_{-0}
$\mathbb{Z}$	2^{+0}_{-0}	3^{+0}_{-0}	5^{+0}_{-1}	5^{+0}_{-1}	2^{+0}_{-0}	3^{+0}_{-0}	4^{+1}_{-0}	4^{+0}_{-0}
$\mathbb{X}$	2^{+0}_{-0}	3^{+0}_{-0}	4^{+1}_{-0}	4^{+1}_{-0}	2^{+0}_{-0}	3^{+0}_{-0}	4^{+0}_{-0}	4^{+0}_{-0}
$\mathbb{F}$	2^{+0}_{-0}	3^{+0}_{-0}	4^{+1}_{-0}	4^{+1}_{-0}	2^{+0}_{-0}	3^{+0}_{-0}	4^{+1}_{-0}	5^{+0}_{-1}
$\mathbb{R}$	2^{+0}_{-0}	3^{+0}_{-0}	4^{+1}_{-0}	5^{+0}_{-0}	2^{+0}_{-0}	3^{+0}_{-0}	4^{+0}_{-0}	4^{+0}_{-0}

Table S.5: Average fidelity $\mathcal{F}$ and purity $\mathcal{P}$ of the channel, $\widetilde{\rho_{\xi*}}$ implemented by a gate $\mathbb{T}$ in d dimensions in the macro-pixel and OAM bases. The standard deviation is calculated from an ensemble of implemented gates with different output foci, and for many realisations for the $\mathbb{R}$ gates.

Basis	$\mathbb{T}$	$\mathcal{F}(\widetilde{\rho_{\xi*}}, \rho_\xi)$				$\mathcal{P}(\widetilde{\rho_{\xi*}})$			
		$d=2$	$d=3$	$d=5$	$d=7$	$d=2$	$d=3$	$d=5$	$d=7$
Macro-Pixel	$\mathbb{I}$	91.7 ± 4.7 %	89.4 ± 5.7 %	78.8 ± 6.3 %	70.0 %*	95.1 ± 1.0 %	97.0 ± 2.4 %	89.7 ± 3.7 %	77.4 %*
	$\mathbb{Z}$	91.8 ± 3.8 %	91.7 ± 4.3 %	75.2 ± 4.2 %	65.2 %*	94.7 ± 1.7 %	97.1 ± 1.3 %	90.2 ± 2.6 %	77.5 %*
	$\mathbb{X}$	91.7 ± 3.6 %	90.5 ± 4.9 %	74.0 ± 5.2 %	59.0 %*	94.7 ± 1.3 %	97.5 ± 1.4 %	88.7 ± 3.5 %	78.7 %*
	$\mathbb{F}$	88.8 ± 3.9 %	86.5 ± 1.9 %	69.6 ± 4.5 %	58.9 %*	89.8 ± 2.5 %	88.3 ± 2.2 %	80.5 ± 2.0 %	75.1 %*
	$\mathbb{R}$	89.2 ± 6.5 %	85.1 ± 3.1 %	72.8 ± 4.6 %	63.5 %*	92.6 ± 2.1 %	88.7 ± 1.8 %	83.1 ± 1.4 %	77.3 %*
OAM	$\mathbb{I}$	88.3 ± 2.0 %	83.5 ± 4.5 %	69.3 ± 4.0 %	54.2 ± 3.0 %	91.2 ± 0.7 %	89.1 ± 2.3 %	81.3 ± 2.2 %	63.6 ± 3.6 %
	$\mathbb{Z}$	88.4 ± 3.4 %	84.5 ± 2.4 %	71.8 ± 5.4 %	48.3 ± 7.6 %	90.2 ± 1.0 %	89.7 ± 1.5 %	81.1 ± 1.2 %	61.5 ± 1.7 %
	$\mathbb{X}$	92.3 ± 2.5 %	82.7 ± 4.8 %	71.9 ± 2.6 %	46.2 ± 4.8 %	93.6 ± 1.5 %	88.4 ± 3.1 %	81.0 ± 1.8 %	61.7 ± 1.3 %
	$\mathbb{F}$	90.3 ± 2.4 %	81.0 ± 5.2 %	69.3 ± 3.0 %	51.7 ± 4.2 %	92.2 ± 1.7 %	85.9 ± 1.8 %	78.8 ± 2.4 %	62.8 ± 2.0 %
	$\mathbb{R}$	90.1 ± 2.6 %	81.4 ± 3.6 %	69.3 ± 3.0 %	47.9 ± 4.4 %	90.5 ± 1.1 %	88.7 ± 4.0 %	79.7 ± 3.3 %	62.0 ± 4.1 %

*The standard deviation is not reported since we only have one realization of the macro-pixel gates in $d = 7$.

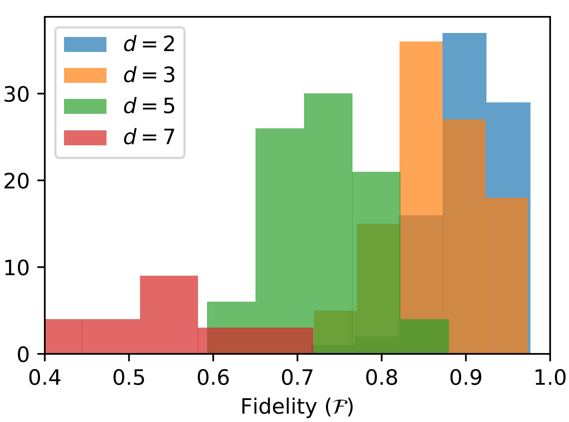

Figure S.4. Histogram of process fidelities of optical circuits implemented in different dimensions.

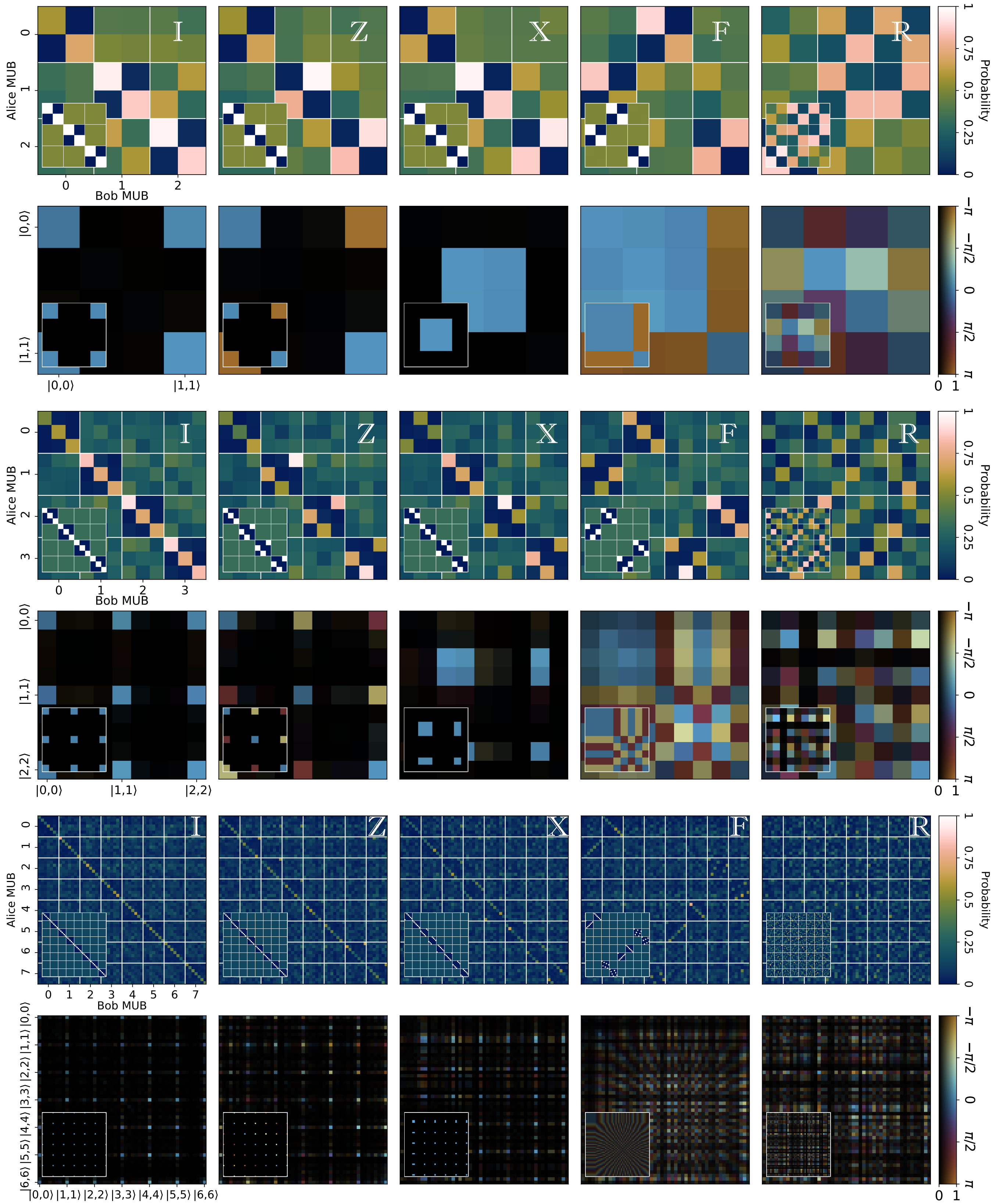

Figure S.5. Manipulation of 2, 3, and 7-dimensional spatially entangled two-photon states in the macro-pixel basis using the $\mathbb{I}$, Pauli-$\mathbb{Z}$, Pauli-$\mathbb{X}$, Fourier $\mathbb{F}$, and random unitary $\mathbb{R}$ gates. In each panel, the upper part shows the two-photon coincidence counts in all MUBs and the lower part depicts reconstructed density matrices of the Choi states $\widetilde{\rho_{\xi*}}$. The density matrix legend captures both the amplitude (brightness, normalised for clarity) and phase (colour).

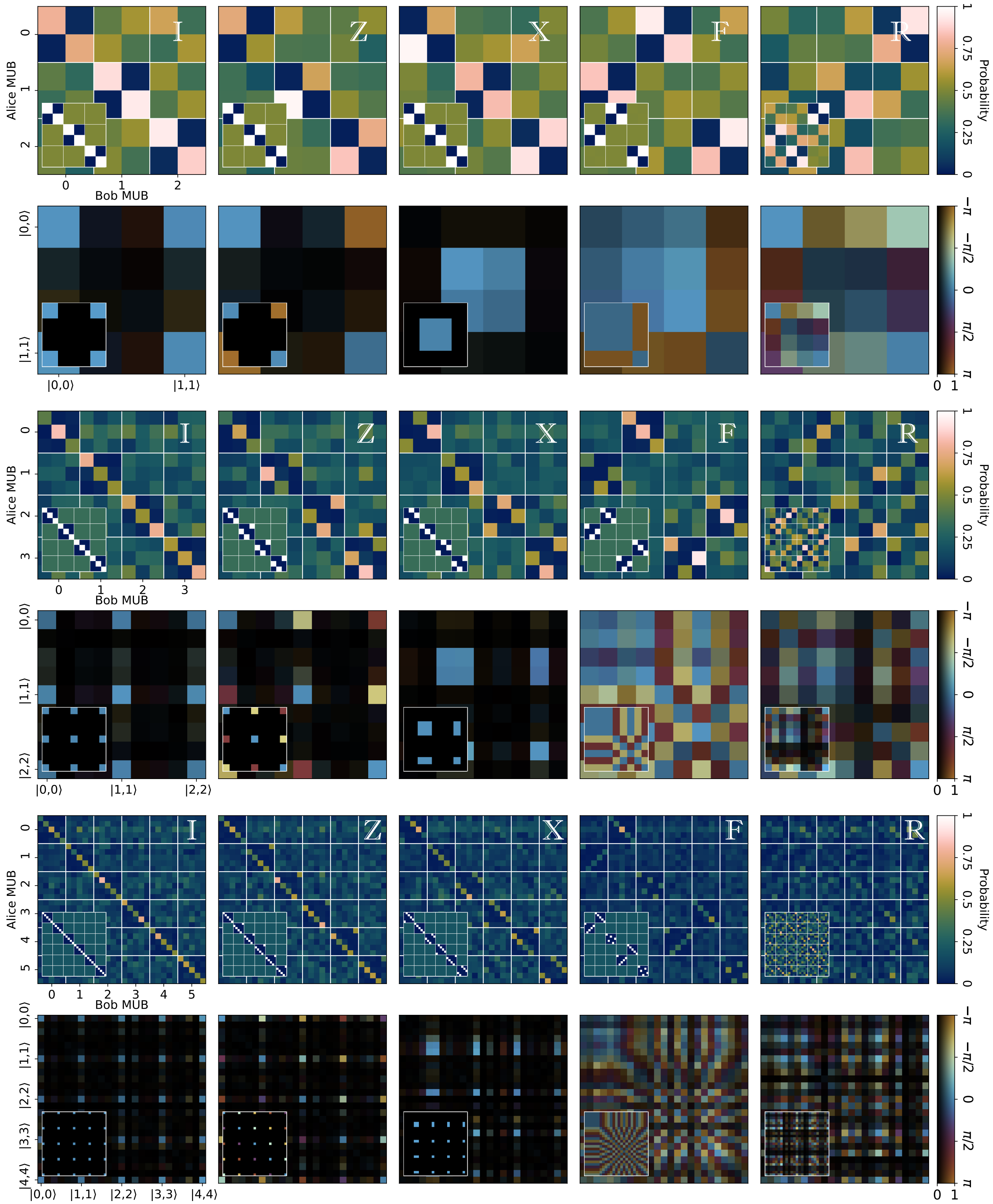

I
Z
X
F
R
Alice MUB
Bob MUB
Probability
0
0.25
0.5
0.75
1
−π
−π/2
π/2
π
|0,0⟩
|1,1⟩
|2,2⟩
|3,3⟩
|4,4⟩

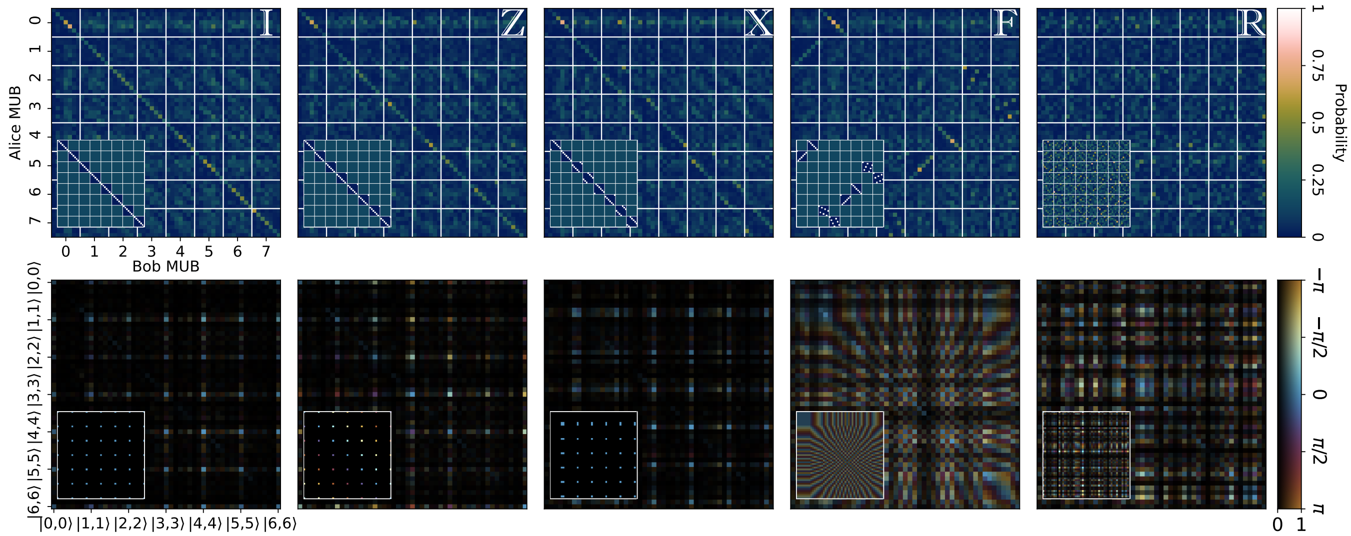

Figure S.6. Manipulation of 2, 3, 5, and 7-dimensional spatially entangled two-photon states in the OAM basis using the $\mathbb{I}$, Pauli-$\mathbb{Z}$, Pauli-$\mathbb{X}$, Fourier $\mathbb{F}$, and random unitary $\mathbb{R}$ gates. In each panel, the upper part shows the two-photon coincidence counts in all MUBs and the lower part depicts reconstructed density matrices of the Choi states $\widetilde{\rho_{\xi *}}$. The density matrix legend captures both the amplitude (brightness, normalised for clarity) and phase (colour).

S.4. Independent characterisation of measurement apparatus and inverse-designed gates

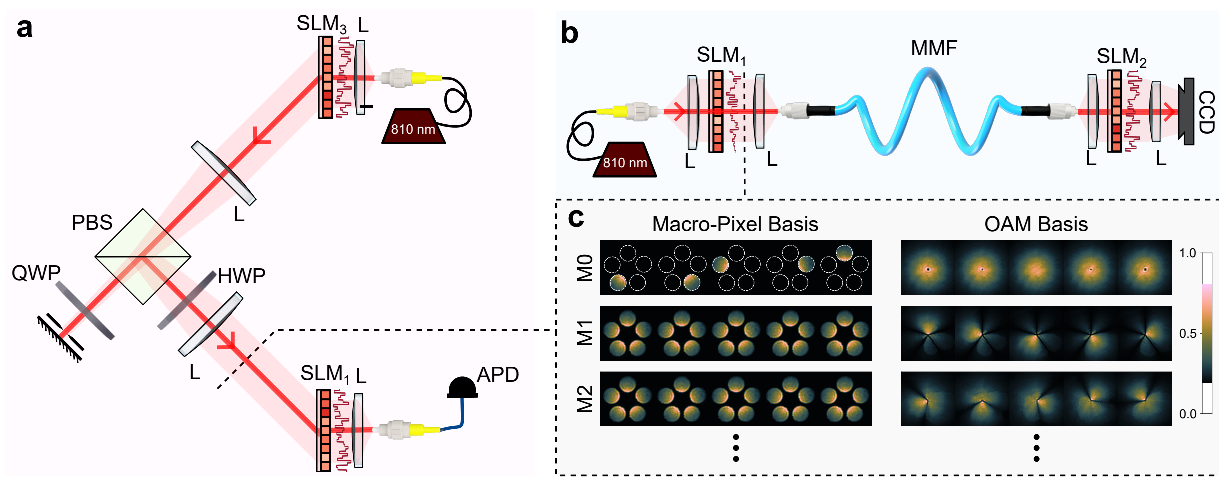

Figure S.7. **Independent characterisation of experiment:** (a) Prepare-and-measure setup implemented in an unfolded two-photon experiment used to characterise our measurement apparatus. (b) Prepare-and-measure setup used to characterise our inverse-designed gates. (c) CCD images of the classical input modes in the macro-pixel and OAM bases used for characterisation.

In this section, we characterise our measurement apparatus and gate transformations independent of our entangled input source. This allows us to study how imperfections in the measurement apparatus limit the quality of our measured states and transformations.

Our measurements are characterised by performing a classical prepare-and-measure experiment in situ in the experimental setup. We unfold our setup about the nonlinear crystal by replacing it with a mirror and analyse it in the Klyshko advanced-wave picture [5]. As shown in Fig. S.7(a), a weak coherent state (superluminiscent diode filtered at $810 \pm 1.5nm$) with the identical wavelength as the entangled photons is back-propagated from the idler photon measurement stage and prepared in a chosen state (precisely those used in our QST measurements). This state is then directed to the signal measurement stage by a mirror placed at the crystal plane, and subsequently projected by the signal photon measurement stage and recorded by an avalanche photo-diode. The measurements performed with the unfolded classical setup are identical to those performed in the main experiment, and allow us to gauge the reduction in the quality of entangled state and gates due to the imperfect measurement apparatus.

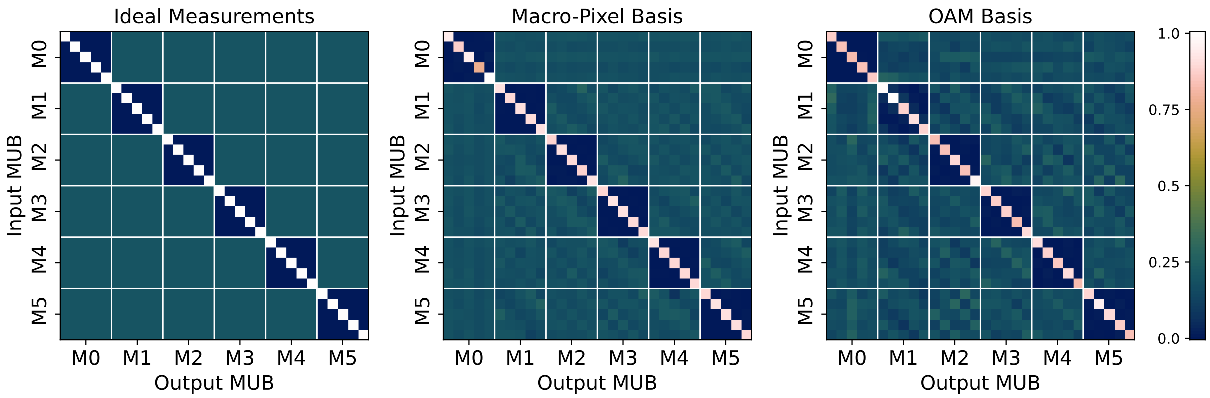

Figure S.8. **Characterisation of measurement apparatus:** Cross-talk matrices corresponding to (a) ideal measurements in the macro-pixel/OAM bases, and imperfect measurements in the (b) macro-pixel basis and (c) OAM basis characterised with a classical prepare-and-measure setup.

Fig. S.8 shows the measured cross-talk matrices for five-dimensional state preparations and measurements for every MUB in the macro-pixel and OAM basis. Fig. S.7(c) shows CCD images of the prepared input modes (image plane denoted by dotted lines in Fig S.7). The imperfections in the coupling matrices can be attributed to misalignments in the experimental setup, as well as imperfections in the computer generated holograms (CGHs) due to pixelisation and non-unit fill fraction. The effect of CGH-induced imperfections can be seen to be more pronounced in the OAM basis since superpositions of modes in this basis require amplitude modulation, while macro-pixel measurements can be performed with phase-only modulation.

Treating these measurements as analogous to (folded) two-photon measurements allow us to upper-bound the quality of a maximally entangled state that can be measured with this setup. We use this procedure to obtain cross-talk matrices in the macro-pixel and OAM bases in $2, 3, 5$, and 7 dimensions. We then perform QST on this data to calculate an upper bound on the fidelity ($\mathcal{F}$) to a maximally entangled state, purity ($\mathcal{P}$), and entanglement dimensionality that can be measured with this setup as shown in Table S.6.

Table S.6: Expected reduction in state purity $\mathcal{P}$, entanglement dimensionality d_{ent}, and fidelity $\mathcal{F}$ of a d-dimensional maximally entangled state due to imperfect measurements characterised using a classical prepare-and-measure experiment. The measured input state fidelities $\mathcal{F}_{\text{exp}}(\rho^{(\text{in})}, \rho^{+})$ from Table S.1 are shown for comparison.

Basis	Dimension (d)	$\mathcal{P}$	d_{ent}	$\mathcal{F}(\rho^{(\text{in})}, \rho^{+})$	$\mathcal{F}_{\text{exp}}(\rho^{(\text{in})}, \rho^{+})$
Macro-Pixel	2	98.99 %	2	99.22 %	96.8 ± 1.4 %
	3	98.28 %	3	98.77 %	95.3 ± 0.4 %
	5	94.26 %	5	96.38 %	91.6 ± 0.6 %
	7	94.76 %	7	90.40 %	83.0 ± 1.2 %
OAM	2	100.0 %	2	99.80 %	97.5 ± 0.2 %
	3	93.06 %	3	96.11 %	90.8 ± 0.6 %
	5	90.15 %	5	94.26 %	86.5 ± 0.7 %
	7	89.91 %	7	93.64 %	80.6 ± 0.6 %

Next, we perform a similar prepare-and-measure experiment on the gate transformations to verify their performance independent of the input entangled state. As shown in Fig. S.7(b), a filtered superluminiscent diode is sent through the programmable circuit consisting of the multimode fiber sandwiched between two SLMs. In this experiment, SLM_1 is used to prepare the classical input states sent into the gates while also contributing to the construction of the gate operation. The output states are measured on a camera, which allows multiple outcomes to be measured simultaneously.

We construct various optical circuits as described in Methods and perform quantum process tomography (QPT) on these gate operations. In order to perform QPT on the gate operation, SLM_2 is used to display the output-mode holograms that correspond to local measurements made by Bob. The resultant data is then processed in the same manner as in AA-QPT, while choosing the input state to be the ideal maximally entangled one, as described in Methods.

Table S.7 shows the performance of these gates. When compared with results shown in Table S.2, one sees that these gates perform better on classical input states than on an entangled input state. This can be attributed to the fact that we use the same classical source (identical wavelength and bandwidth) to characterise our fiber transmission matrix. In addition, slight differences in alignment can result in imperfect mode-matching between our input entangled state and classical light source.

Table S.7: Measured fidelity $\mathcal{F}$ and purity $\mathcal{P}$ of inverse-designed gates using a classical prepare-and-measure experiment.

Basis	$\mathbb{T}$	$\mathcal{F}(\widetilde{\rho_{\xi*}}, \rho_\xi)$				$\mathcal{P}(\widetilde{\rho_{\xi*}})$			
		$d=2$	$d=3$	$d=5$	$d=7$	$d=2$	$d=3$	$d=5$	$d=7$
Macro-Pixel	$\mathbb{I}$	98.4 %	98.7 %	94.7 %	84.7 %	97.4 %	100.0 %	98.2 %	86.0 %
	$\mathbb{Z}$	98.4 %	99.1 %	94.5 %	84.0 %	98.2 %	99.6 %	94.5 %	88.9 %
	$\mathbb{X}$	98.6 %	99.4 %	95.3 %	83.3 %	100.0 %	100.0 %	98.5 %	83.3 %
	$\mathbb{F}$	96.9 %	90.5 %	89.3 %	81.4 %	96.1 %	90.8 %	88.8 %	79.2 %
	$\mathbb{R}$	97.4 %	93.3 %	88.1 %	79.0 %	96.3 %	92.0 %	86.4 %	73.7 %
OAM	$\mathbb{I}$	96.8 %	91.3 %	81.3 %	66.7 %	93.8 %	87.5 %	82.5 %	71.8 %
	$\mathbb{Z}$	97.0 %	89.9 %	82.3 %	68.6 %	94.8 %	87.8 %	79.9 %	67.1 %
	$\mathbb{X}$	95.5 %	89.9 %	77.5 %	71.4 %	92.4 %	86.6 %	71.2 %	67.5 %
	$\mathbb{F}$	97.0 %	90.6 %	82.1 %	68.8 %	96.0 %	86.2 %	82.2 %	68.3 %
	$\mathbb{R}$	96.6 %	90.7 %	80.5 %	67.3 %	94.0 %	90.0 %	78.2 %	64.1 %

S.5. Errors in QST and AA-QPT due to the measurement apparatus

When performing QST and AA-QPT, errors in the measurement apparatus can lead to erroneous state reconstruction [6], which often tends to be the systematic type. As demonstrated above in S.4, the measurements in our laboratory conditions are not perfect, so here we address the problem by using the above prepare-and-measure experiment to estimate the distribution of errors in our measurement settings, and use these to estimate the consequent errors in state and process reconstruction using QST and AA-QPT.

The prepare-and-measure experiment described in S.4 is repeated 50 times, following realignment procedures used in the actual experiment. The realignment consists of performing a knife-edge scan to find the center of incident beams on the SLM, as well as performing a raster-scan on the fiber facet by displaying different gratings on the SLM. In each trial, the tomography of measurements is used to fit model parameters pertaining to the experimental sources of misalignment, i.e. tilt and displacement of projected optical fields on the SMF, as shown in Fig. S.9(a). The results of these fitted experimental parameters are presented in histograms Fig. S.9(b), which provide distributions of the experimental misalignments. Given these distributions, we perform error propagation by numerically sampling from the ensemble of misalignments and calculating the resultant imperfect measurement projectors ($\widetilde{\hat{\Pi}}_i$), which correspond to the actual measurement errors that can occur in our experiment.

To assess the resultant estimation errors on our QST/AA-QPT fidelity, fidelity to target state, and state purity, we simulate the effects of these measurement errors on our experimentally estimated state, $\widetilde{\rho}_*$, in the following manner. For QST, given an estimated state $\widetilde{\rho}_*$, in the ith trial we generate a sample measurement, $\widetilde{\hat{\Pi}}_i$, from the ensemble of misaligned measurements containing a set of tomographic measurement projectors. We calculate the measured detection statistics of $\widetilde{\hat{\Pi}}_i$ on $\widetilde{\rho}_*$, and perform the QST reconstruction via SDP to obtain a recovered state estimate, $\widetilde{\rho}_i$. For AA-QPT, we first perform this sampling procedure to generate the input state, then repeat the procedure for Choi state estimation using that particular input state sample. We repeat these steps 200 times, and record the QST/AA-QPT fidelities, $\{\mathcal{F}(\widetilde{\rho}_i, \widetilde{\rho}_*)\}_i$, the fidelities to target state $\{\mathcal{F}(\widetilde{\rho}_i, \rho^{\text{target}})\}_i$, and the purities $\{\mathcal{P}(\widetilde{\rho}_i)\}_i$. These

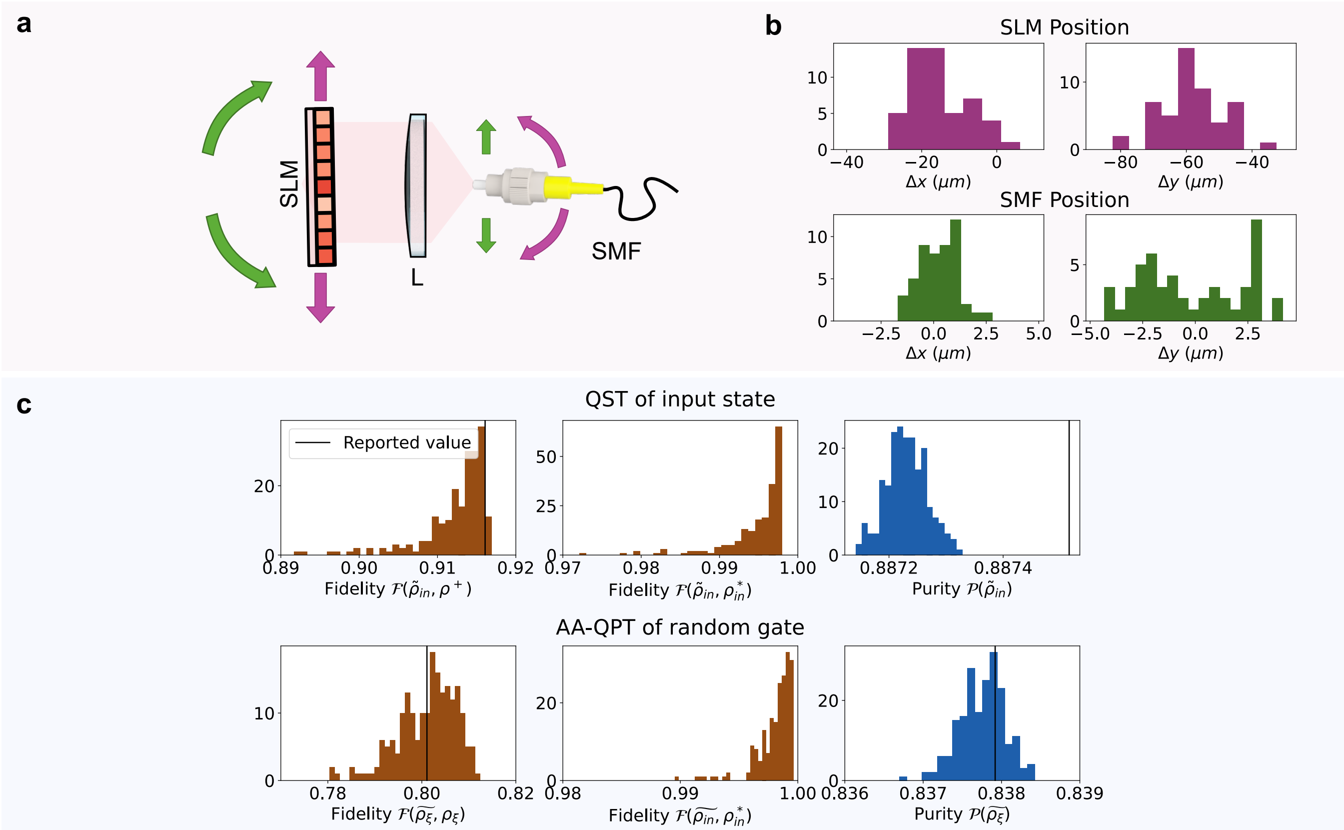

Figure S.9. **Misalignment-induced systematic errors**: (a) Sources of misalignment in spatial single-outcome projective measurements performed with a spatial light modulator (SLM), lens (L), and a single-mode fiber (SMF). (b) Histograms of errors in positions of holograms displayed on the SLM and positions of the SMF. The misalignments are characterised using multiple prepare-and-measure experiments. (c) Histograms of errors propagating through QST and AA-QPT in fidelity and purity of states and processes. Here we show the example of a 5-dimensional entangled state and a random-unitary gate in the macro-pixel basis. The black lines indicate the values reported in the main experiment.

distributions then correspond to the measurement errors of our actual state estimation procedure, providing that the ground-truth state (which we cannot know) undergoes similar reconstruction errors to the state estimate $\widetilde{\rho_*}$.

The fidelity of QST (AA-QPT), the fidelity to the target (target Choi) state, and the purity are presented in Fig. S.9(c), for QST of the 5-dimensional macro-pixel entangled input state and AA-QPT of the 5-dimensional Random gate. These show representative behaviour of the sampling procedure. Complete results for each estimated state are presented in Fig. S.10 and Fig. S.11. We also mark the corresponding property of the underlying experimental state estimate, $\widetilde{\rho_*}$, as black lines in Fig. S.9(c).

For the 5-dimensional input state, we find that the fidelity of the QST procedure, exemplified by $\{\mathcal{F}(\widetilde{\rho_i}, \widetilde{\rho_*})\}_i$, has sample mean fidelity 99.48% indicating a slight infidelity of QST caused by the measurement error. For the fidelity to the maximally entangled target state ($\{\mathcal{F}(\widetilde{\rho_i}, \rho^{\text{target}})\}_i$), we observe that measurement errors almost exclusively lead to a reduction, demonstrating that the measurement errors likely cause systematically an underestimation of the true initial state quality. The standard error of this fidelity to target state, $\Delta_M = 0.57\%$, is calculated with respect to the underlying state fidelity ($\mathcal{F}(\widetilde{\rho_*}, \rho^{\text{target}})$), and we conservatively cite this as the symmetric error on our recorded fidelities in the main text. Similarly, the purity of the recovered state under these measurement errors ($\{\mathcal{P}(\widetilde{\rho_i})\}_i$) almost exclusively decreases (albeit very slightly), leading to a likely underestimation of state purity, though we again cite this standard deviation in the main text and Table S.1, and these results are summarised in Table S.8.

For AA-QPT, where both the input state and the recovered Choi state are sampled as above, we observe somewhat different behaviours. The fidelity of the AA-QPT procedure for a 5-dimensional random gate, $\{\mathcal{F}(\widetilde{\rho_{\xi i}}, \widetilde{\rho_{\xi *}})\}_i$ has a sample mean of 99.81% indicating reasonably stable process recovery given our measurement errors. The fidelity to target Choi state shows a broadened distribution featuring both over- and under-estimation of fidelity to target Choi state (unlike the QST case), with a standard deviation $\Delta_M = 0.62\%$. The purity of the recovered Choi states is also broadened about the underlying Choi state purity $\mathcal{P}(\widetilde{\rho_{\xi *}})$. We cite the standard deviation with respect to the measured values in the main text and Table S.2 and summarise in Table S.8.

In some cases, particularly where the input state basis suffers more detrimental impurity caused by measurement errors than the output state, we can observe a slight systematic tendency to over-estimate Choi state fidelities and purities. This discrepancy between QST and AA-QPT behaviours can be explained by noting that an over-estimation of noise in an input state would lead to misattribution of output state noise to the input state and not to the Choi state, thus under-estimating Choi state noise. We demonstrate this effect symbolically when performing a direct inversion to solve for the Choi state in the case of white noise mixing of the input state in Supplementary S.6.

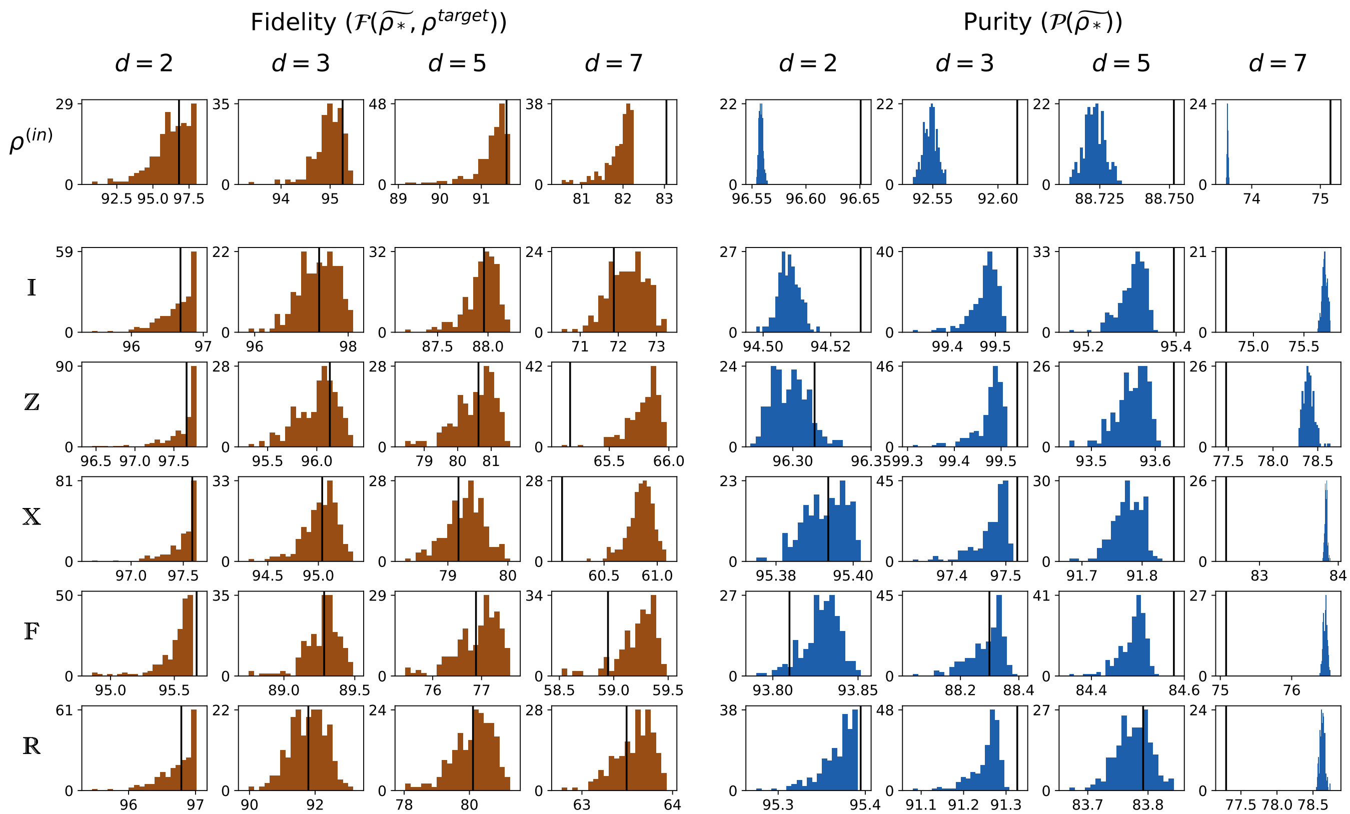

Figure S.10. **Measurement error analysis for macro-pixel basis**: Histogram of fidelity and purity of reconstructed input state $\rho^{(\mathrm{in})}$ using QST as well as quantum gates reported in Table S.2 using AA-QPT, with respect to the reported values (black line).

S.6. Misestimation of initial state in linear inversion

Perfect recovery of the underlying Choi state of a channel requires accurate estimation of the initial state. Suppose the true initial state given by Eqs. 8 were misestimated by,

$$\rho^{(\mathrm{in,\ noise})}(p) = \big(p\mathcal{A} \otimes \mathbb{I} + (1-p)\mathcal{B} \otimes \mathbb{I}\big)(\rho^{+}) \tag{S.6.1}$$

where $\mathcal{B}$ is some additive noise. When attempting the linear inversion of the Choi state, ρ_{ξ}, it would be misestimated by,

$$\rho_{\xi*}(p) = \big(p\mathcal{A} \otimes \mathbb{I} + (1-p)\mathcal{B} \otimes \mathbb{I}\big)^{-1}\big(\mathcal{A} \otimes \mathbb{I}\big)\rho_{\xi} \tag{S.6.2}$$

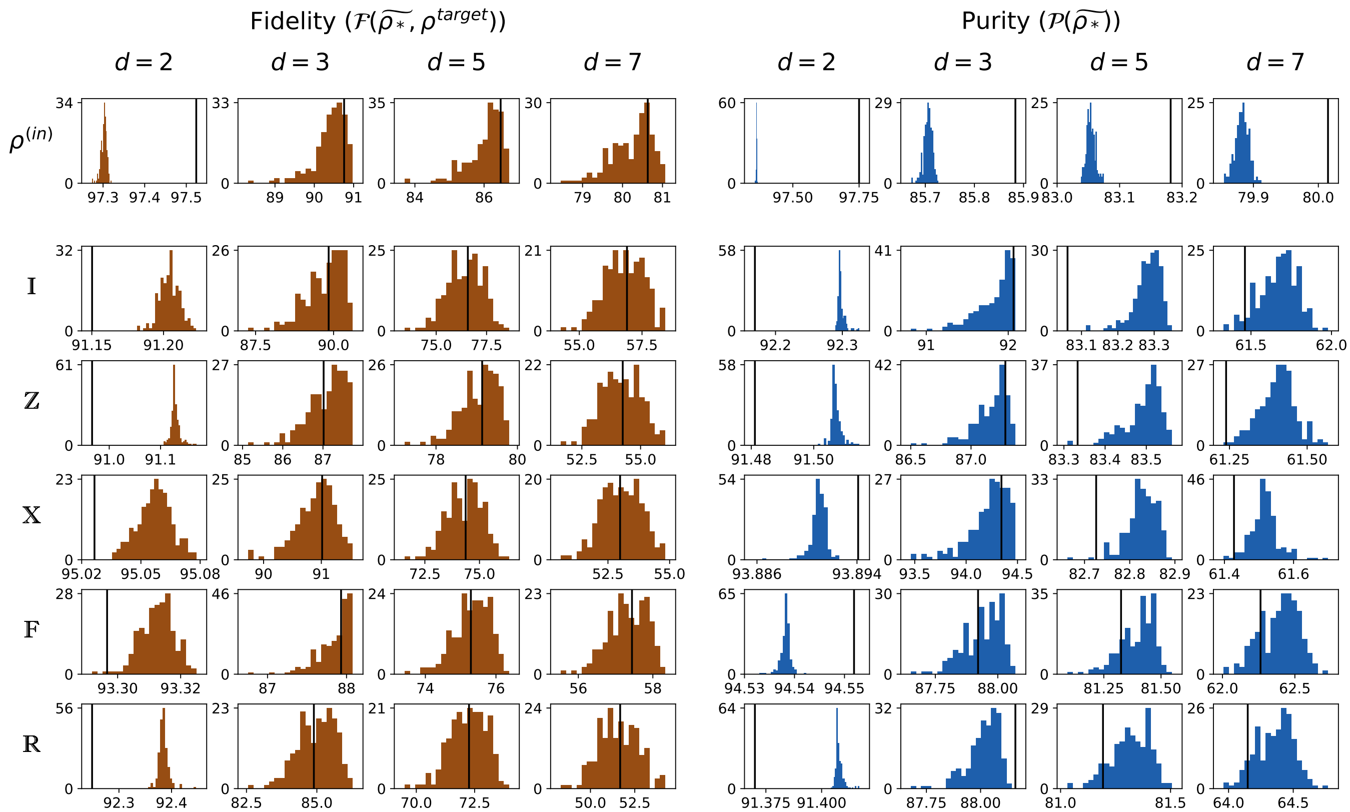

Figure S.11. **Measurement error analysis for OAM basis**: Histogram of fidelity and purity of reconstructed input state $\rho^{(\mathrm{in})}$ using QST as well as quantum gates reported in Table S.2 using AA-QPT, with respect to the reported values (black line).

which may be unphysical. In the case of additive white noise, $\mathcal{B} \otimes \mathbb{I}$ is rank one (in the sense that its matrix representation when acting on vectorised states has rank one). We use the Sherman–Morrison formula to arrive at,

$$\begin{aligned}
\rho_{\xi*}(p) &= \big(p\mathcal{A} \otimes \mathbb{I} + (1-p)\mathcal{B} \otimes \mathbb{I}\big)^{-1}\big(\mathcal{A} \otimes \mathbb{I}\big)(\rho_\xi) \\
&= \left(\tfrac{1}{p}\mathcal{A}^{-1} \otimes \mathbb{I} - \tfrac{(1-p)}{p^2} g(\mathcal{A}^{-1} \otimes \mathbb{I})(\mathcal{B} \otimes \mathbb{I})(\mathcal{A}^{-1} \otimes \mathbb{I})\right)\big(\mathcal{A} \otimes \mathbb{I}\big)(\rho_\xi) \\
&= \tfrac{1}{p}\rho_\xi - \left(\tfrac{(1-p)}{p^2} g(\mathcal{A}^{-1} \otimes \mathbb{I})(\mathcal{B} \otimes \mathbb{I})\right)(\rho_\xi) \\
\text{where} \quad g &:= \frac{1}{1 + \frac{1-p}{p}\mathrm{Tr}[\mathcal{B} \otimes \mathbb{I} \mathcal{A}^{-1} \otimes \mathbb{I}]}
\end{aligned} \tag{S.6.3}$$

If the initial state were maximally entangled, $\mathcal{A} = \mathbb{I}$, then the second term in Eqs. S.6.3 subtracts (potentially filtered) white noise, $\mathcal{B} \otimes \mathbb{I}(\rho_\xi)$, from the true Choi state, leading to a resultant over-estimation of the channel purity. Assessing the systematic errors presented by misestimation of our initial state in our tomographic protocols is the subject of Supplementary S.5

S.7. Programmability and scalability of top-down designed circuits

To investigate the programmability and scalability of our approach, we numerically construct many instances of the high-dimensional circuits by varying our design parameters, i.e., dimension of circuit d, dimension of mode-mixers n, depth of circuit L, using the model

$$\mathbf{T} := U_{L+1} \prod_{j=1}^{L} P_j U_j, \tag{S.7.4}$$

Table S.8: Results of errors from photon counting statistics and imperfect measurement settings on the input state, $\rho^{(\mathrm{in})}$ in QST and the Choi states of gates, ρ_ξ, in AA-QPT. We report the sample mean of the QST/AA-QPT fidelities ($\overline{\mathcal{F}(\widetilde{\rho}_i, \widetilde{\rho}_*)}$), and the one standard deviation Poisson error (Δ_P) and measurement error (Δ_M) of the fidelity to target state ($\mathcal{F}(\widetilde{\rho}_*, \rho^{\mathrm{target}})$) and purity ($\mathcal{P}(\widetilde{\rho}_*)$).

Basis	State	$\overline{\mathcal{F}(\widetilde{\rho}_i, \widetilde{\rho}_*)}$ (%)				$\Delta\mathcal{F}(\widetilde{\rho}_*, \rho^{\mathrm{target}})$ (%)								$\Delta\mathcal{P}(\widetilde{\rho}_*)$ (%)							
		$d=2$	$d=3$	$d=5$	$d=7$	$d=2$		$d=3$		$d=5$		$d=7$		$d=2$		$d=3$		$d=5$		$d=7$	
						Δ_P	Δ_M	Δ_P	Δ_M	Δ_P	Δ_M	Δ_P	Δ_M	Δ_P	Δ_M	Δ_P	Δ_M	Δ_P	Δ_M	Δ_P	Δ_M
Macro-Pixel	$\rho^{(\mathrm{in})}$	99.66	99.72	99.48	96.64	0.12	1.42	0.08	0.41	0.06	0.57	0.06	1.20	0.22	0.09	0.15	0.07	0.11	0.03	0.10	1.50
	$\rho_{\mathbb{I}}$	99.89	99.88	99.80	99.63	0.85	0.25	0.52	0.41	0.68	0.16	0.96	0.60	0.45	0.02	0.26	0.07	0.39	0.10	0.64	0.98
	$\rho_{\mathbb{Z}}$	99.89	99.89	99.82	99.59	0.85	0.24	0.45	0.24	0.78	0.61	0.75	0.63	0.44	0.02	0.25	0.07	0.50	0.07	0.48	0.92
	$\rho_{\mathbb{X}}$	99.89	99.89	99.80	99.56	0.78	0.18	0.67	0.17	0.95	0.33	0.67	0.75	0.41	0.01	0.36	0.06	0.58	0.08	0.38	1.27
	$\rho_{\mathbb{F}}$	99.87	99.90	99.83	99.70	0.93	0.21	0.84	0.12	0.97	0.44	0.66	0.32	0.51	0.02	0.49	0.06	0.60	0.09	0.43	1.39
	$\rho_{\mathbb{R}}$	99.87	99.89	99.81	99.70	0.64	0.27	0.54	0.55	0.94	0.62	0.71	0.22	0.33	0.03	0.29	0.08	0.53	0.03	0.39	1.34
OAM	$\rho^{(\mathrm{in})}$	99.78	99.44	99.19	98.78	0.04	0.22	0.04	0.55	0.03	0.69	0.02	0.65	0.08	0.39	0.06	0.18	0.06	0.13	0.05	0.13
	$\rho_{\mathbb{I}}$	99.98	99.57	99.65	99.51	0.39	0.05	0.38	0.61	0.41	0.90	0.47	0.79	0.19	0.13	0.21	0.32	0.24	0.22	0.28	0.24
	$\rho_{\mathbb{Z}}$	99.98	99.63	99.62	99.55	0.31	0.16	0.38	0.47	0.45	0.46	0.53	0.82	0.17	0.03	0.20	0.18	0.28	0.17	0.30	0.17
	$\rho_{\mathbb{X}}$	99.98	99.56	99.64	99.53	0.45	0.03	0.39	0.35	0.40	0.81	0.44	0.80	0.25	0.00	0.22	0.23	0.24	0.11	0.26	0.10
	$\rho_{\mathbb{F}}$	99.98	99.73	99.66	99.53	0.43	0.02	0.43	0.22	0.46	0.50	0.44	0.53	0.24	0.01	0.24	0.08	0.27	0.10	0.25	0.19
	$\rho_{\mathbb{R}}$	99.98	99.68	99.65	99.58	0.51	0.14	0.42	0.66	0.44	0.78	0.48	1.10	0.28	0.04	0.22	0.16	0.23	0.15	0.24	0.26

where the n reconfigurable phase elements at each P_j are found using the wavefront-matching algorithm as explained in Methods given a set of $n \times n$ unitary matrices $\{U_j\}_j$ and a set of d input and output modes of interest. The codes for these simulations are available in [7]. Once a circuit is implemented, we classify its performance by measuring fidelity (Eq. 12) and success probability (Eq. 13). For a given set of design parameters n, L and d, we implement multiple realisations of the Identity $\mathbb{I}$, Pauli-$\mathbb{X}$, Pauli-$\mathbb{Z}$, Fourier-$\mathbb{F}$, and random unitary $\mathbb{R}$ gates (Eq. 6), by varying the set of d input and output modes of interest which are randomly selected. We simulate these circuits by treating the mode-mixers $\{U_j\}_j$ as either a set of random unitaries or discrete Fourier transforms (DFT).

As presented in the main text, when the dimension of the circuit, d, is less than the dimension of mode-mixers, n ($d/n < 0.1$), both fidelity and success probability reduce as the circuit dimension increases. Fig. S.12 conveys these trends in detail. For all these realisations, all random mode-mixers $\{U_j\}$ correspond to the same random unitary matrix, and the positions of input/output modes of interest are randomly selected for each implementation. The behaviour reported in Fig. S.12 is also observed either when different random mode-mixers are used in each layer, or input/output modes are specifically assigned to the first d modes of the U_j. Interestingly, the same trends for fidelity and success probability are observed for all gate types, indicating that there is no advantage when programming specific types of gates using this method. The same holds for both DFT and random mode-mixers with randomly selected inputs and outputs, indicating that a DFT is similar to a random unitary in this regime.

For a circuit described by Eq. S.7.4, the total number of degrees of freedom (DOFs) is given by the number of reconfigurable elements nL. On the other hand, the constraint on the number of DOFs required to program a d-dimensional circuit $\mathbb{T}$ is $\mathcal{O}(d^2)$ [8, 9]. A larger d leads to loss of performance because the number of DOFs required to program the circuit increases. Thus, as d increases, the number of reconfigurable elements does not change. Improving the figures of merit of a d-dimensional circuit can therefore be addressed in two primary ways: increasing the dimension of mode-mixers, n, or the depth of circuit, L.

To study the region where the fidelity and success probability converge to unity, we have plotted our simulation data on a log-log plot (Fig. S.13), replacing fidelity with infidelity $(1-F)$ and success probability with failure probability $(1-S)$. As shown in Fig. S.13a, the infidelity converges to zero (capped at 10^{-16} due to the floating-point precision used) when the total number of reconfigurable elements exceeds the number required to program a unitary operation ($\mathcal{O}(d^2)$). The point at which $(1-F) \to 0$ depends on the ratio of d/n. In the case where $d = n$, the number of reconfigurable elements required is optimal, and the infidelity rapidly converges to zero. In the regime where $d/n < 1$ however, the number of elements necessary for full programmability increases as d/n decreases. For instance, when $d/n < 0.1$ the infidelity converges to zero slower as a function of the number of elements (normalised by dimension). In Fig. S.13b, we observe that the failure probability decreases as a function of the circuit depth and rapidly converges to zero (capped at 10^{-16}) when $L \approx \mathcal{O}(d)$ in all cases of $d \leq n$. In this regime, full programmability is achieved and is seen to be relatively independent of d/n. Note that the failure probability for $d = n$ is always zero.

These results show that in order to achieve both high fidelity and success probability, one does not need to solely rely on the number of reconfigurable elements, but also on their distribution across the circuit. Ideally, one would want to implement a fully programmable circuit using the full dimension of mode-mixers ($d = n$) constructed from 2×2 beam splitters or $n \times n$ mode-mixers, since this achieves the minimum number of reconfigurable elements [10, 11]. However, it is known that in the presence of imperfections, an increase in the depth of the circuit is required to improve the fidelity in such schemes [12–14]. Scaling the depth of circuit in practice may nonetheless not be the most viable option due to a variety of experimental reasons, namely, propagation and interface losses and accumulation of errors. Instead of considering errors and scattering losses as a problem, the top-down approach presents a reasonable alternative ($d < n$ and $L \lesssim \mathcal{O}(d)$) where randomness is exploited to implement a circuit with a low depth. Here, both fidelity and success probability are acceptably high, while n can increase to improve the fidelity without reducing the success probability from unity when $L > 2d$, or with a trade-off on the success probability when $L \leq 2d$. Many optical devices, for instance, computer-generated holograms and MPLC devices [15, 16] can be considered to fall in this category where mode-mixing can be implemented by free-space propagation, a $2f$ lens system, or another transformation such as a circulant matrix [17, 18].

Finally, while the deterministic construction of programmable circuits from discrete Fourier transforms is known for $d = n$ [19, 20], a proof of universal programmability of unitary circuits using random-unitary mode-mixers remains open to the best of our knowledge, and the deterministic construction of such circuits is yet to be discovered.

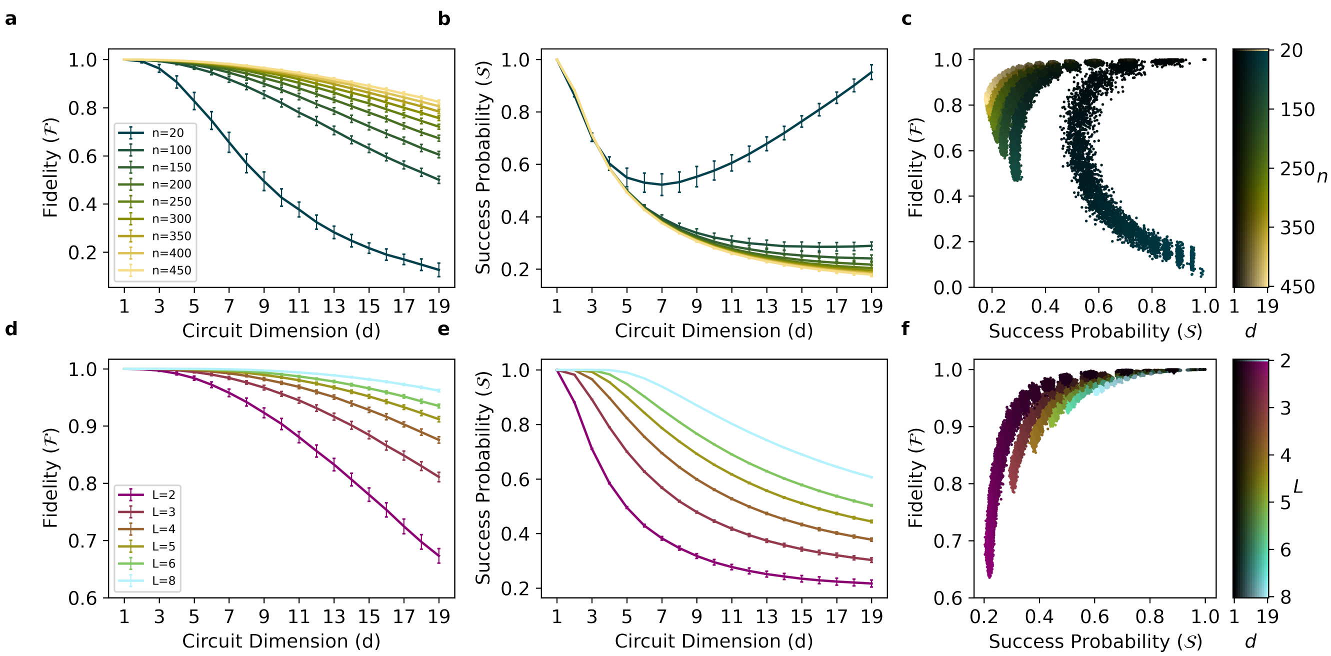

Figure S.12. **Simulated fidelity $\mathcal{F}$ and success probability $\mathcal{S}$ for all gates implemented in a circuit with random unitary mode-mixers**: (a-c) $\mathcal{F}$ and $\mathcal{S}$ as a function of the dimension of mode-mixers, n, with a circuit depth $L = 2$ and (d-f) $\mathcal{F}$ and $\mathcal{S}$ as function of circuit depth L while using mode-mixers with dimension $n = 200$. A sample size of 200 is used to derive the statistics of each data-point. The data is presented as mean values ±1 standard deviation.

S.8. Effects of randomness and symmetry

A pertinent point to address is the role that randomness plays in the implementation of an optical circuit using the top-down approach. For instance, instead of having a random unitary evolution between phase planes, one could have another transformation such as a discrete Fourier transform (DFT) or a circulant matrix, which normally have a symmetric structure [17, 18]. In practice, such transformations can be difficult to implement on an integrated platform, normally requiring a high degree of accurate control. Due to inherent imperfections and bending, a commercial multi-mode fiber is much closer to a random matrix in our basis of interest than a symmetric transformation. In this section, we investigate the effect of randomness on the gates performance, by comparing circuit implementations using random

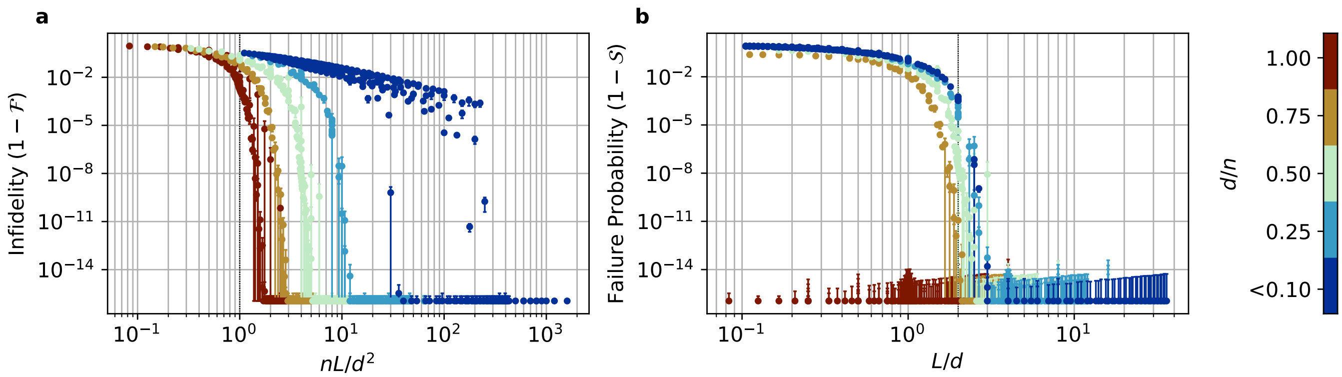

Figure S.13. Infidelity $1-\mathcal{F}$ (a) and failure probability $1-\mathcal{S}$ (b) for simulated gates implemented in a circuit with random-unitary mode-mixers. Minimum values are capped at 10^{-16} since this corresponds to the floating-point precision in our simulation.A sample size of 96 is used to derive the statistics of each data-point. The data is presented as mean values ±1 standard deviation.

unitary mode-mixers ($\{U_j\}_j = R$) with ones using discrete Fourier transforms (DFT) ($\{U_j\}_j = F$), given that the set of input/output modes of interest are fixed to be the first d modes of the U_j. This is to be contrasted with the randomly selected input/output modes in S.7, where there is no difference in performance between circuits with random and DFT mode-mixers.

The fidelity and success probability of random gates of different circuit dimension using a random unitary mode-mixer and a DFT mode-mixer are compared in Fig. S.14. We observe that for a low number of circuit layers ($L < 4$), the random unitary mode-mixer performs better in terms of fidelity. However, this comes with a lower success probability than achievable with a DFT mode-mixer. At $L \geq 4$, there is no difference in performance between the two types of circuit, as in this regime, the combination of several DFTs and phase planes starts approaching a random structure itself. In general, one can expect that implementing circuits with symmetry will be better with a mode-mixer that has some inherent symmetry. For example, a DFT transformation is certainly easier to perform with a DFT mode-mixer. However, as pointed out above, such mode-mixers can be difficult to implement in practice as compared with random unitary mode-mixers.

It is known that a symmetry present on a unitary U reduces the number of free parameters, consequently resulting in fewer reconfigurable elements needed in their implementation. For example, the number of optical elements required for ($d = 2^k$)-dimensional discrete Fourier transform is $(d/2)\log_2 d$ where k is a positive integer [21, 22]. The use of symmetric mode-mixers thus brings both pros for implementing a particular circuitry and cons for full programmablity. Regardless, random mode-mixers are easier to find and use in practice, simply requiring a system with some inherent randomness such as an imperfect multi-mode fiber. In addition, they are more suitable for implementing a fully programmable circuit, and provide the added benefit of a large ambient mode-mixer dimension, which further increases circuit fidelity.

[1] Vatshal Srivastav, Natalia Herrera Valencia, Saroch Leedumrongwatthanakun, Will McCutcheon, and Mehul Malik, *Characterizing and tailoring spatial correlations in multimode parametric down-conversion,* Physical Review Applied **18**, 054006 (2022), arXiv:2110.03462.

[2] Jessica Bavaresco, Natalia Herrera Valencia, Claude Klöckl, Matej Pivoluska, Paul Erker, Nicolai Friis, Mehul Malik, and Marcus Huber, *Measurements in two bases are sufficient for certifying high-dimensional entanglement,* Nature Physics **14**, 1032 (2018), 1709.07344.

[3] Natalia Herrera Valencia, Vatshal Srivastav, Matej Pivoluska, Marcus Huber, Nicolai Friis, Will McCutcheon, and Mehul Malik, *High-Dimensional Pixel Entanglement: Efficient Generation and Certification,* Quantum **4**, 376 (2020), arXiv:2004.04994.

[4] Natalia Herrera Valencia, Vatshal Srivastav, Saroch Leedumrongwatthanakun, Will McCutcheon, and Mehul Malik, *Entangled ripples and twists of light: radial and azimuthal Laguerre–Gaussian mode entanglement,* Journal of Optics **23**, 104001 (2021), arXiv:2104.04506.

[5] D N Klyshko, *A simple method of preparing pure states of an optical field, of implementing the Einstein–Podolsky–Rosen experiment, and of demonstrating the complementarity principle,* Soviet Physics Uspekhi **31**, 74 (1988).

[6] Denis Rosset, Raphael Ferretti-Schöbitz, Jean-Daniel Bancal, Nicolas Gisin, and Yeong-Cherng Liang, *Imperfect measurement settings: Implications for quantum state tomography and entanglement witnesses,* Phys. Rev. A **86**, 062325 (2012).

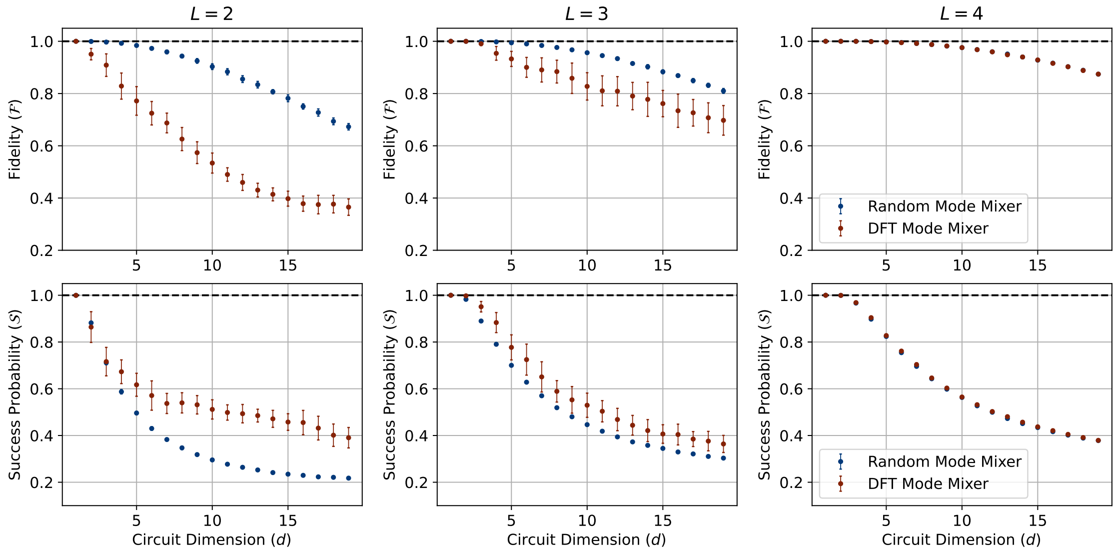

Figure S.14. **Comparison of fidelity ($\mathcal{F}$) and Success probability ($\mathcal{S}$) of random gates implemented with random-unitary mode-mixers ($U_j = R$) and DFT mode-mixers ($U_j = F$) with dimension** $n = 200$**, for different number of layers ($L = 2, 3, 4$).** A sample size of 27 is used to derive the statistics of each data-point. The data is presented as mean values ±1 standard deviation.

.

[7] Suraj Goel, Saroch Leedumrongwatthanakun, Natalia Herrera Valencia, Will McCutcheon, Claudio Conti, Pepijn W. H. Pinkse, and Mehul Malik, *Simulation codes for : Inverse-design of high-dimensional quantum optical circuits in a complex medium,* (2022).

[8] Unter, Z. I. Borevich, and S. L. Krupetskii, *Subgroups of the unitary group that contain the group of diagonal matrices,* Journal of Soviet Mathematics **17**, 1951 (1981).

[9] David A B Miller, *How complicated must an optical component be?* Journal of the Optical Society of America A **30**, 238 (2013).

[10] Michael Reck, Anton Zeilinger, Herbert J Bernstein, and Philip Bertani, *Experimental realization of any discrete unitary operator,* Physical Review Letters **73**, 58 (1994).

[11] William R. Clements, Peter C. Humphreys, Benjamin J. Metcalf, W. Steven Kolthammer, Ian A. Walsmley, and Ian A. Walmsley, *Optimal design for universal multiport interferometers,* Optica **3**, 1460 (2016), arXiv:1603.08788.

[12] David A. B. Miller, *Perfect optics with imperfect components,* Optica **2**, 747 (2015).

[13] Roel Burgwal, William R. Clements, Devin H. Smith, James C. Gates, W. Steven Kolthammer, Jelmer J. Renema, and Ian A. Walmsley, *Using an imperfect photonic network to implement random unitaries,* Optics Express **25**, 28236 (2017), arXiv:1612.01199.

[14] Sunil Pai, Ben Bartlett, Olav Solgaard, and David A. B. Miller, *Matrix Optimization on Universal Unitary Photonic Devices,* Physical Review Applied **11**, 064044 (2018), 1808.00458.

[15] Jean-François Morizur, Lachlan Nicholls, Pu Jian, Seiji Armstrong, Nicolas Treps, Boris Hage, Magnus Hsu, Warwick Bowen, Jiri Janousek, and Hans-A Bachor, *Programmable unitary spatial mode manipulation,* Journal of the Optical Society of America A **27**, 2524 (2010), arXiv:1005.3366.

[16] Pauline Boucher, Arthur Goetschy, Giacomo Sorelli, Mattia Walschaers, and Nicolas Treps, *Full characterization of the transmission properties of a multi-plane light converter,* Physical Review Research **3**, 023226 (2020), 2005.11982.

[17] Michael Schmid, Rainer Steinwandt, Jörn Müller-Quade, Martin Rötteler, and Thomas Beth, *Decomposing a matrix into circulant and diagonal factors,* Linear Algebra and Its Applications **306**, 131 (2000).

[18] Marko Huhtanen and Allan Perämäki, *Factoring Matrices into the Product of Circulant and Diagonal Matrices,* Journal of Fourier Analysis and Applications **21**, 1018 (2015).

[19] Martin Idel and Michael M. Wolf, *Sinkhorn normal form for unitary matrices,* Linear Algebra and Its Applications **471**, 76 (2015), arXiv:1408.5728.

[20] Víctor López Pastor, Jeff Lundeen, and Florian Marquardt, *Arbitrary optical wave evolution with Fourier transforms and phase masks,* Optics Express **29**, 38441 (2021), arXiv:1912.04721.

[21] P. Törmä, I. Jex, and S. Stenholm, *Beam splitter realizations of totally symmetric mode couplers,* Journal of Modern Optics **43**, 245 (1996).

[22] Ronen Barak and Yacob Ben-Aryeh, *Quantum fast Fourier transform and quantum computation by linear optics,* Journal

of the Optical Society of America B **24**, 231 (2007).